# Resonant Two-Laser Spin-State Spectroscopy of a Negatively Charged Quantum-Dot–Microcavity System with a Cold Permanent Magnet

P. Steindl,[1,*] T. van der Ent,[1] H. van der Meer,[1] J.A. Frey,[2] J. Norman,[3] J.E. Bowers,[3] D. Bouwmeester,[1,2] and W. Löffler[1,†]

[1] *Huygens-Kamerlingh Onnes Laboratory, Leiden University, P.O. Box 9504, 2300 RA Leiden, Netherlands*
[2] *Department of Physics, University of California, Santa Barbara, Santa Barbara, California 93106, USA*
[3] *Department of Electrical and Computer Engineering, University of California, Santa Barbara, Santa Barbara, California 93106, USA*

(Received 4 March 2023; revised 18 May 2023; accepted 12 June 2023; published 13 July 2023)

A high-efficiency spin-photon interface is an essential piece of quantum hardware necessary for various quantum technologies. Self-assembled (In,Ga)As quantum dots have excellent optical properties: if embedded in an optical microcavity, they can show near-deterministic spin-photon entanglement and spin readout. To address the individual spin states, an external magnetic field is required, and a superconducting magnet is usually used. Here we show a compact cryogenically compatible Sm-Co magnet design that delivers a 475-mT in-plane (Voigt-geometry) magnetic field at 5 K, which is suitable for lifting the energy degeneracy of the electron spin states and trion transitions of a single (In,Ga)As quantum dot. This quantum dot is embedded in a birefringent high-finesse optical microcavity that enables efficient collection of single photons emitted by the quantum dot. We demonstrate spin-state manipulation by addressing the trion transitions with a single laser field and two laser fields. The experimental data agree well with our model, which covers single- and two-laser cross-polarized resonance fluorescence, Purcell enhancement in a birefringent cavity, and variation of the laser powers.

DOI: 10.1103/PhysRevApplied.20.014026

## I. INTRODUCTION

An efficient, tunable spin-photon interface that allows high-fidelity entanglement of spin qubits with flying qubits, photons, lies at the heart of many building blocks of distributed quantum technologies [1]—ranging from quantum repeaters [2] and photonic gates [3,4] to the generation of photonic cluster states [5–7]. Further, to secure connectivity within the quantum network, an ideal spin-photon interface requires near-unity collection efficiency. Therefore an atom or semiconductor quantum dot (QD) carrying a single spin as a quantum memory is integrated into photonic structures such as optical microcavities, where recently 57% in-fiber photon-collection efficiency was achieved [8].

Within the pool of promising systems, singly charged excitonic complexes of optically active QD devices in III-V materials [9] combine near-unity quantum efficiency and excellent zero-phonon-line emission at cryogenic temperatures [10] with a nearly-lifetime-limited optical linewidth [11]. This, in combination with subnanosecond Purcell-effect-enhanced lifetimes, enabled gigahertz-scale generation rates of indistinguishable single photons [8,12–17], robust polarization selection rules [18,19], and simple on-chip integration facilitating stable-long term operation and tunability.

The singly charged QD can be optically excited to the trion state. If this is done with linearly polarized light, the spin state of the resident electron is transferred to the trion hole spin by the optical selection rules. If the trion decays, it will emit a single circularly polarized photon with a helicity depending on the hole spin state; see Fig. 1(a). To achieve selective spin addressability, which is necessary for spin initialization and readout, the QD is typically placed in an external in-plane (Voigt-geometry) magnetic field [20,21], which induces Zeeman splitting of the spin states and trion transitions [18]. The magnetic field modifies the eigenstates of the system and the optical selection rules, and four optical transitions are possible [see Fig. 1(b)], which are now linearly polarized. The electron and trion spin, as well as the photon polarization, are now connected by the modified optical selection rules. We obtain two intertwined $\Lambda$ systems that can be used with steady-state light fields for spin initialization [20,21], the generation of arbitrary superposition of spin ground states [22], or dynamical spin decoupling from the nuclear bath [23].

*steindl@physics.leidenuniv.nl
†loeffler@physics.leidenuniv.nl

 

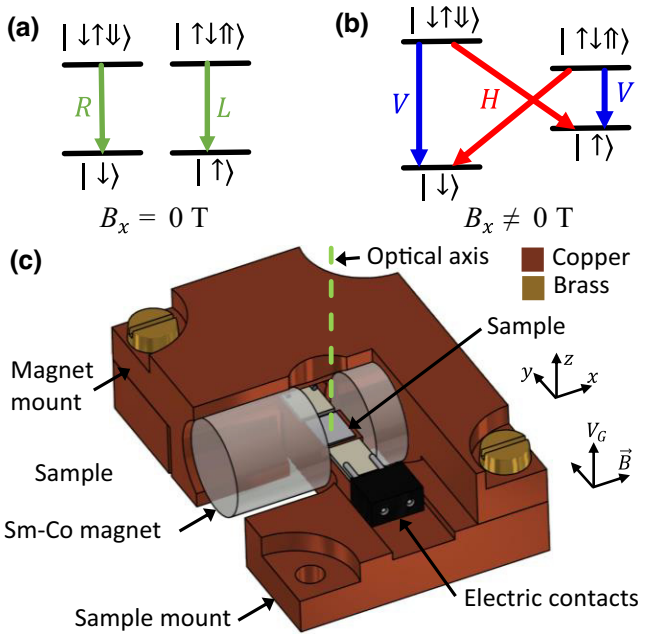


FIG. 1. Energy-level schemes of a negatively charged QD and the magnetic assembly. Optical selection rules for trion transitions (a) without and (b) with an external in-plane magnetic field. Arrows represent the photon emission of a photon with horizontal ($H$), vertical ($V$), left-circular ($L$), and right-circular ($R$) polarization. (c) Cutaway schematic of the permanent-magnet assembly.

Spin manipulation is more difficult if the QD is coupled to a polarization nondegenerate birefringent microcavity [8,17,24], since the orientation of the in-plane magnetic field needs to be aligned with a cavity polarization axis, and the Purcell enhancement of the QD transitions becomes polarization dependent. Here we report resonant two-laser spectroscopy [21,25] of a single spin in a single QD in such a birefringent cavity, and use cross-polarized collection of single photons. We use a simple cryogenic permanent-magnet assembly to apply the magnetic field, and we are able to derive the spin dynamics by comparison with a theoretical model.

## II. PERMANENT MAGNET ASSEMBLY

Magneto-optical QD-based experiments usually rely on large and complex superconducting magnets [7,26], which generate strong magnetic fields but require both a stabilized current source and cryogenic temperatures. However, many experiments need only a static magnetic field of around 500 mT, which can be achieved with compact strong permanent magnets cooled down together with the QD device [27–29]. Unfortunately, many rare-earth magnetic materials, such as (Nd,Fe)B [30], suffer at cryogenic temperatures from spin reorientation [31], which lowers the effective magnetic field [32] and tilts the easy axis of the magnetic assembly [30,33]. Especially, losing control over the magnetic field direction is problematic with QDs since it affects mixing between dark and bright states and thus changes both transition energies and optical selection rules [34].

To build our permanent-magnet assembly, we chose from the strongest commercially available magnetic materials [35,36] Sm-Co (grade 2:17) magnets with a room-temperature remanence of 1.03 T. This industrially used magnetic system is known for its high Curie temperature (more than 800 °C) and high magnetocrystalline anisotropy [37,38], which are excellent for high-temperature applications in several fields [39–41]. Especially it is used above the Curie temperatures of (Nd,Fe)B of 310 °C [38], where current (Nd,Fe)B-based magnets have relatively poor intrinsic magnetic properties. Moreover, because of the low temperature dependence of remanence and coercivity [36,42,43], Sm-Co-based magnets also show excellent thermal stability of the remanence with near-linear dependence [32,42] down to 4.2 K. This is in contrast to other common rare-earth magnet compounds such as (Nd,Fe)B [30], where the remanence at temperatures below 135 K, depending on the specific material composition [32], decreases rapidly by several percent due to the spin-reorientation transition [31].

Our permanent-magnet assembly in Fig. 1(c) is designed to fit on top of an $X$-$Y$-$Z$ piezoelectric motor assembly in a standard closed-cycle cryostat with optical access via an ambient-temperature long-working-distance objective, which restricts its height to approximately 1 cm. Thus, we build the assembly from two $9 \times 9$ mm$^2$ commercially available rod-shaped Sm-Co magnets separated by a 4.5-mm air gap embedded in a $36 \times 24 \times 10.8$ mm$^3$ copper housing. Because of the large remanence (1.03 T) and small air gap, the assembly in the center of the gap produces a homogeneous magnetic field of about 500 mT, as discussed in Sec. S1 in Supplemental Material [44]. The assembly is rigidly attached by brass screws to the H-shaped copper sample mount, where the QD device is horizontally placed in the center of the air gap such that the magnetic field is in the plane (Voigt geometry). The assembly contains electrical contacts to apply a bias voltage $V_G$ to the device. It has a low weight of 69 g (including 4.8 g per magnet), which is compatible with standard nanopositioners allowing fine-tuning of the sample position with respect to the optical axis.

The magnetic mount is then cooled down together with the sample to approximately 5 K. Since in Sm-Co, the spin-reorientation transition was reported to be stable down to 10 K [32], we do not expect magnetization-axis changes and assume only a small magnetic field drop of 5% between room temperature and cryogenic temperature [30]. This makes Sm-Co an ideal material choice for strong homogeneous cryogenic magnets, in our case delivering about 475 mT at 5 K.

## III. SPIN-STATE DETERMINATION

We study self-assembled (In,Ga)As QDs emitting at a wavelength λ of around 935.5 nm, embedded in an approximately-λ-thick GaAs planar cavity, surrounded by two distributed Bragg reflectors: 26 pairs of λ/4-thick GaAs/$Al_{0.90}Ga_{0.10}As$ layers at the top and 13 pairs of GaAs/AlAs layers and 16 pairs of GaAs/$Al_{0.90}Ga_{0.10}As$ layers at the bottom [24,46]. The single QD layer is embedded in a *p-i-n* junction, separated from the electron reservoir by a 31.8-nm-thick tunnel barrier including a 21.8-nm-thick $Al_{0.45}Ga_{0.55}As$ electron-blocking layer designed to allow single-electron charging of the QD [47,48]. A voltage bias $V_G$ applied over the diode allows charge control of the ground state of the QD and also fine-tuning of the QD transition energies into resonance with the optical-cavity mode. The in-plane optical-cavity-mode confinement is achieved by ion etching of eight circular trenches arranged in an octagon into the top distributed Bragg reflector down to a 10-nm-thick AlAs layer. By oxidation of this layer, an intracavity lens or aperture is formed, which leads to transverse mode confinement. Details of the device are discussed in Sec. S3 in Supplemental Material [44]. We fabricate 216 cavities per device [49] and select a suitable one with (i) a QD well coupled to the cavity mode and (ii) low birefringence of the fundamental mode; for the device studied here, the two linearly polarized cavity modes (horizontally and vertically polarized modes) are split by $\Delta_c = 28$ GHz.

First, we cool down the device to 5 K without the Sm-Co-magnet assembly in a closed-cycle cryostat. For resonant laser spectroscopy, we use a cross-polarization laser extinction method with laser rejection greater than $10^6$ [50]. With use of a free-space polarizer and a half-wave plate, the polarization of the excitation laser beam is aligned along the vertical cavity polarization axis, and the light reflected from the cavity is recorded with a single-photon detector after it passes again through the half-wave plate and the crossed polarizer. In Fig. 2(a), we show a fluorescence map of this device measured in the cross-polarization scheme as a function of the laser-frequency detuning from the vertically-polarized-cavity-mode resonance $\Delta f_l$ and the applied bias voltage $V_G$. We observe a single emission line that is shifted by the quantum-confined Stark effect. The line is in resonance with the vertically polarized cavity mode at around 1.25 V and with the horizontally polarized cavity mode at around 1.40 V. The same line is visible also if the excitation polarization and detection polarization are swapped; see the cross-section plot in Fig. 2(c). The fact that we observe the same single line under both perpendicular polarizations and that it is coupled to both fundamental cavity modes suggests that the emitted photons are circularly polarized and originate from the charged exciton $X^-$.

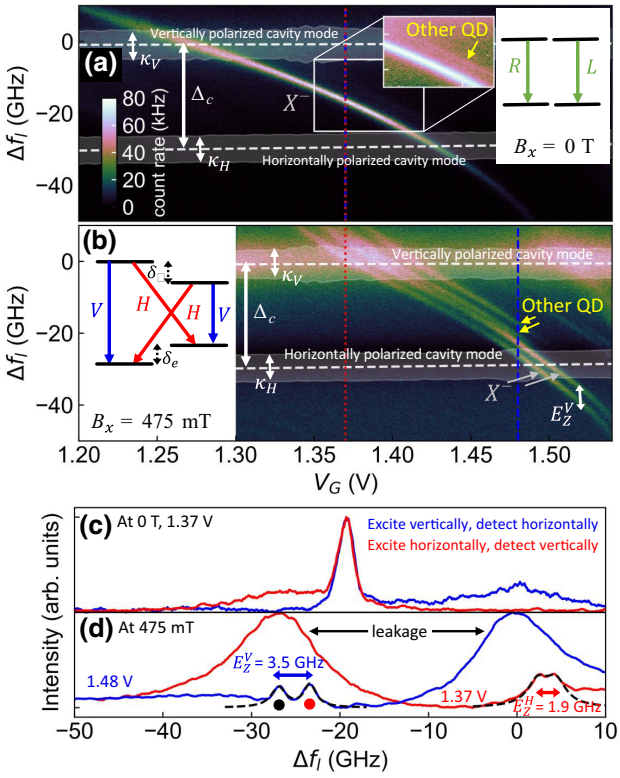


FIG. 2. Resonant reflection as a function of laser frequency and gate voltage (a) without and (b) with an in-plane external magnetic field, plotted with the same color scale. The excitation laser beam is polarized along the vertical cavity axis and reflected laser light is filtered out by a crossed horizontal polarizer to select photons emitted by the QD trion. Insets show the corresponding optical selection rules. Dashed lines indicate the cavity resonance frequencies, and the cavity linewidth given by the decay rates $\kappa_V$ and $\kappa_H$ are shown highlighted; both are determined by semiclassical-model fits [45]. The data in the inset in (a) are plotted on a logarithmic scale. In (c),(d) cross-section plots without and with a magnetic field for two excitation polarizations (blue for excitation along the vertical cavity axis, and red for excitation along the horizontal cavity axis) at voltages of 1.37 V or 1.48 V, indicated by the vertical lines in (a),(b), are shown. The Zeeman splittings determined from Lorentzian fits (dashed black lines) are given. The excitation power in front of the excitation objective is 2 nW and the laser scanning speed is 41 GHz/s.

We next cool down the device with the Sm-Co-magnet assembly, to lift the energy degeneracy of the trion transitions. In this scenario, with the energy-level scheme in Fig. 2(b), the optical selection rules are modified by the in-plane magnetic field from circular to linear polarization. Thus, the scanning excitation laser beam polarized along the vertical cavity axis can only resonantly address vertically polarized transitions, i.e., $|\downarrow\rangle \rightarrow |\downarrow\uparrow\Downarrow\rangle$ and $|\uparrow\rangle \rightarrow |\uparrow\downarrow\Uparrow\rangle$, and therefore we expect to observe a

pair of lines Zeeman-split by energy $E_Z^V = \delta_e + \delta_h$. Without cavity enhancement, each of the excited trion states radiatively decays with equal probability (by cavity Purcell enhancement—however, this is modified) into the single-spin ground state by emission of a single photon with either vertical or horizontal polarization depending on the excited and ground states, as depicted in Fig. 2(b). Because we measure in cross-polarization, we filter out the emitted vertically polarized single photons and detect only photons emitted by the $|{\downarrow}{\uparrow}{\Downarrow}\rangle \rightarrow |{\uparrow}\rangle$ and $|{\uparrow}{\downarrow}{\Uparrow}\rangle \rightarrow |{\downarrow}\rangle$ transitions. Thus, the total detected rate is reduced to half of that without a magnetic field. Similarly, the scanning laser beam polarized along the horizontal cavity axis excites only $|{\uparrow}\rangle \rightarrow |{\downarrow}{\uparrow}{\Downarrow}\rangle$ and $|{\downarrow}\rangle \rightarrow |{\uparrow}{\downarrow}{\Uparrow}\rangle$, and we observe again a pair of fluorescence lines, this time Zeeman-split by $E_Z^H = |\delta_e - \delta_h|$. Note that in Fig. 2(b) we observe two pairs of emission lines that originate from two different QDs. We focus only on the brighter QD, corresponding to the clear transition in Fig. 2(a). In agreement with the trion energy-level scheme, the trion transitions exhibit a different Zeeman splitting of $E_Z^V = 3.5 \pm 0.1$ GHz under vertical-polarization excitation and $E_Z^H = 1.9 \pm 0.1$ GHz under horizontal-polarization excitation. This Zeeman splitting is extracted by Lorentzian fits (linewidth approximately 1.5 GHz) to the laser-frequency scans shown in Fig. 2(d), which allows us to estimate [51] the electron and hole $g$ factors. We obtain $|g_e| = 0.39$ and $|g_h| = 0.12$; these values agree with literature values for small (In,Ga)As QDs [52]. We also observe a 25-GHz average energy shift of the QD emission caused by a combination of the diamagnetic shift (around 0.5 GHz, assuming a diamagnetic constant of $-9.4$ $\mu$eV/T$^2$ [25]) and temperature- and/or strain-induced band-gap changes between consecutive cooldowns. These changes are likely also responsible for the brightness change of the second QD, which is hardly visible in Fig. 2(a). Note that we also observe a broad emission, which is most likely due to nonresonant cavity-enhanced QD transitions [53,54] in combination with imperfect polarization alignment and/or filtering [50].

## IV. TWO-COLOR RESONANT LASER EXCITATION

We now demonstrate spin-state manipulation using two individually tunable narrow-linewidth lasers. For a high-degree cross-polarization extinction ratio, we perform resonance fluorescence spectroscopy in the vicinity of the horizontally polarized cavity mode ($V_G = 1.49$ V). We use vertical polarization of the beams of both excitation lasers to solely address the transitions marked by dots in Fig. 2(d). These transitions show Zeeman splitting larger than the QD linewidth, leading to frequency labeling of the spin states, which we use to address the spin states.

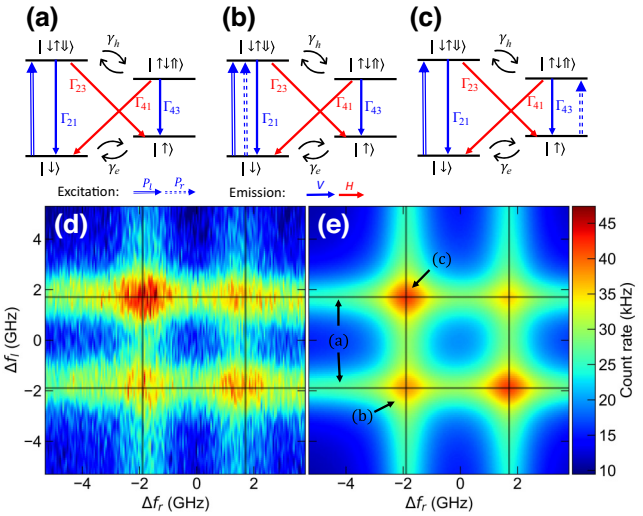


FIG. 3. Two-color laser trion spectroscopy with a magnetic field in Voigt geometry. (a)–(c) Comparison of three different trion excitation conditions: (a) single-laser excitation; (b) two same-frequency lasers; (c) two different-frequency lasers where each laser addresses a different trion transition. (d) Experiment and (e) model data for two-color experiments, for pump-laser power $P_l = 2.1$ nW and repump-laser power $P_r = 2.0$ nW. The black lines indicate the QD trion transition frequencies.

In Fig. 3(d), we show a reflection map measured in cross-polarization as a function of both laser frequencies $f_l$ (pump) and $f_r$ (repump). The horizontal and vertical lines indicate the trion transition frequencies. Where these frequencies intersect, interesting dynamics occurs. First, the nodes oriented along the diagonal represent a condition where both lasers are resonant with the same transition, corresponding to the excitation scheme depicted in Fig. 3(b). We call this configuration "two-laser resonant excitation." The system dynamics under this excitation is equivalent to that under single-laser resonant excitation (1LRE), with stronger emission due to the higher driving power of $P_l + P_r$. The antidiagonally oriented nodes correspond to emission under two-color excitation, where each laser pumps a distinct transition [Fig. 3(c)]; we refer to this scheme as "two-color resonant excitation" (2CRE) [25]. For clarity, we further focus only on the situation where the first laser of constant power $P_l$ continuously pumps the $|{\downarrow}\rangle \rightarrow |{\downarrow}{\uparrow}{\Downarrow}\rangle$ transition. Because of cross-polarization detection, we observe only horizontally polarized emission from the $|{\downarrow}{\uparrow}{\Downarrow}\rangle \rightarrow |{\uparrow}\rangle$ transition, a signature of population shelving into the $|{\downarrow}\rangle$ spin state. This shelved population is repumped, and thus the total (detected) single-photon rate increases by repumping the $|{\uparrow}\rangle \rightarrow |{\uparrow}{\downarrow}{\Uparrow}\rangle$ transition with the second laser, and we observe a higher photon rate at the antidiagonal nodes in Fig. 3(d).

To gain more-precise knowledge of the magnitude of the spontaneous decay rates $\Gamma_{xy}$ as well as the electron and hole spin-flip rates $\gamma_e$ and $\gamma_h$ involved in the system

dynamics, we compare our experiments with a model that is derived in Sec. S5 in Supplemental Material [44]. For a laser power below the saturation power $P_c$, the model is derived from the rate equations describing the steady-state two-scanning-lasers' pump of the trion energy scheme in Fig. 3. The trion transitions are modeled as two coupled $\Lambda$ systems with different vertically polarized and horizontally polarized radiative transition rates due to cavity enhancement of the latter. A careful analysis of the model parameters and comparison with our experimental results allows us to determine the electron spin-flip rates $\gamma_e$ to be approximately 2.5 MHz, while the hole spin-flip rate cannot be determined because of the short lifetime of the excited trion states, as expected. Further, we obtain lifetimes $\Gamma_{21} = 2.1$ GHz, $\Gamma_{43} = 2.7$ GHz, and $\Gamma_{23} = \Gamma_{41} = 0.8$ GHz. Similar spin-flip rates were reported in earlier resonant two-color trion spectroscopy without a cavity [25]; the cavity-enhanced radiative rates $\Gamma_{21}$ and $\Gamma_{43}$ agree with our power-broadening analysis, where we expect a relaxation rate of about 3 GHz for a spectral width of 1.5 GHz; see Sec. S4 in Supplemental Material [44]. Note that the cavity-enhanced rates $\Gamma_{21}$ and $\Gamma_{43}$ are different due to different Purcell enhancement of the transitions, while the nonenhanced rates $\Gamma_{23}$ and $\Gamma_{41}$ are identical, as expected [18,25].

Figure 4 shows the spin-flip-rate dependency of the steady-state occupation of the trion and electron spin states predicted by our theory. In the simulation with vary $\gamma_e$ and we use the system parameters found as reported above together with laser powers $P_l = 2.1$ nW and $P_r = 2.0$ nW to demonstrate spin pumping. First, if the electron spin-flip rate is small (below 1 kHz), the weak pump laser pumping the transition $|\downarrow\rangle \rightarrow |\downarrow\uparrow\Downarrow\rangle$ initializes the spin state $|\uparrow\rangle$. By optical repumping with the second laser on resonance with $|\uparrow\rangle \rightarrow |\uparrow\downarrow\Uparrow\rangle$, the shelved spin population can be largely transferred from $|\uparrow\rangle$ into $|\downarrow\rangle$, as demonstrated in Figs. 4(c) and 4(d). Because of the optical repumping, the resonant absorption on spin $|\uparrow\rangle$ becomes possible again, leading experimentally to the recovery of the transmission signal at the resonant frequency with $|\downarrow\rangle \rightarrow |\downarrow\uparrow\Downarrow\rangle$ [25,55]. Our simulation for the determined spin-flip rate $\gamma_e$ of approximately 2.5 MHz shows that the electron spin flip leads to a comparable spin population of both ground states even without a repumping laser field, making conclusive absorption measurements difficult because of the small change between ground-state populations with and without optical repumping. However, the spin repumping from $|\uparrow\rangle$ is accompanied by the population of $|\uparrow\downarrow\Uparrow\rangle$, resulting in extra emission from this spin state. Importantly, the presence of this extra emission is independent of the ground-state spin-flip rate and can thus be used as a signature of optical spin repumping. Moreover, at low $\gamma_e$, the emission following the spin repumping benefits also from the extra excited-state population of the state $|\downarrow\uparrow\Downarrow\rangle$; see Fig. 4(a).

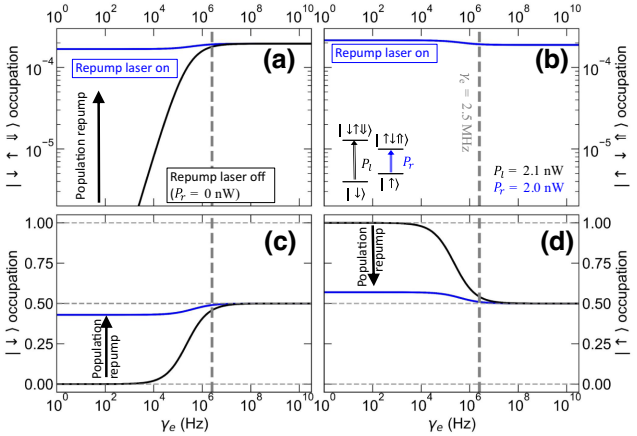


FIG. 4. Occupation probability of (a),(b) steady-state trion states and (c),(d) electron ground-state spin as a function of electron spin-flip rate with (blue) and without (black) the repump laser. The dashed lines show the determined spin-flip rate $\gamma_e \approx$ 2.5 MHz.

Finally, we test our model against the results of a series of excitation-power-dependent experiments shown in Fig. 5. Both observed trion transitions under 1LRE [black and red symbols corresponding to lines in Fig. 2(d)] show saturation with power described by 180 kHz/$(1 + P_c/P)$ [46,56] with a reasonable saturation power $P_c = 22 \pm 2$ nW, in agreement to our model.

In contrast to these single-frequency measurements, the 2CRE scheme shown by the blue symbols in Fig. 5 shows clear signs of spin repumping: because of the continuous repumping of the spin population of both ground

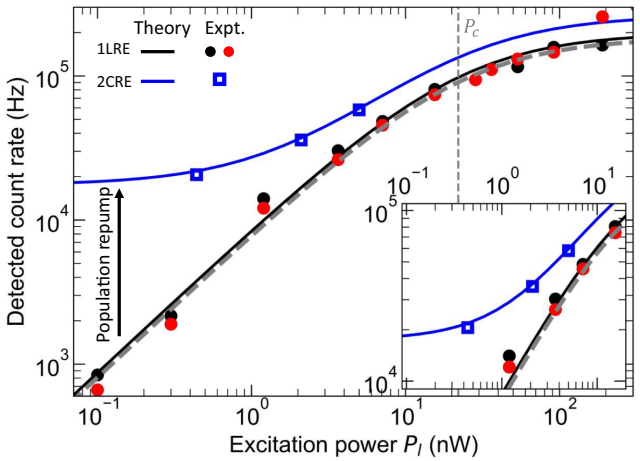


FIG. 5. Power dependency of the trion resonant fluorescence under different excitation schemes, comparing experimental photon count rates (symbols) with rates from our model (lines) with $\gamma_e = 2.5$ MHz: only one pump laser for both trion transitions (1LRE, black and red) and with the repump laser (2CRE, blue). The dashed gray lines indicate the saturation behavior of the two-level system.

states with the two lasers (at constant $P_r = 2.0$ nW), we control the individual steady-state spin populations by altering the relative power of the lasers. Because higher repumping power leads to stronger repumping and thus to higher excited-state occupation, we experimentally observe increased photon rates, following our model predictions. This increase varies with the relative powers of the pump-laser and repump-laser beams from a factor greater than 10 at $P_l = 0.44$ nW to a factor of 1.3 above $P_c$.

## V. CONCLUSIONS

We develop a compact cryogenic Sm-Co-permanent-magnet assembly delivering an in-plane magnetic field of 475 mT. In contrast to superconducting solenoids, this solution does not need any active control and works from cryogenic temperature to ambient temperature. Therefore, we believe it could become a preferable, economical, and scalable architecture for spin-photon interfaces where the magnetic field is used in "set-and-forget" mode.

Using this magnetic assembly in Voigt geometry, we show Zeeman splitting and spin addressability of the electron and trion states of a negatively charged quantum dot embedded in a birefringent optical microcavity. We demonstrate spin-state manipulation using continuous-wave resonant two-laser spectroscopy, which in combination with a high-extinction-ratio cross-polarization technique enables background-free single-photon readout. This two-laser excitation scheme, which is similar to earlier schemes [21,22,25] without a cavity, will allow spin-state initialization and manipulation.

In principle, a weaker permanent magnet can be used to avoid frequency labeling of the polarization states in spin-photon-entanglement experiments [7,57].

## ACKNOWLEDGMENTS

We acknowledge funding from the European Union's Horizon 2020 research and innovation program under Grant Agreement No. 862035 (QLUSTER), from FOM-NWO (Grant No. 08QIP6-2), from NWO-OCW as part of the Frontiers of Nanoscience program, from the Quantum Software Consortium, from Quantum Delta NL, and from the National Science Foundation (Grants No. 0901886 and No. 0960331).

[1] D. D. Awschalom, R. Hanson, J. Wrachtrup, and B. B. Zhou, Quantum technologies with optically interfaced solid-state spins, Nat. Photon. **12**, 516 (2018).

[2] H. J. Kimble, The quantum internet, Nature **453**, 1023 (2008).

[3] K. Koshino, S. Ishizaka, and Y. Nakamura, Deterministic photon-photon $\sqrt{\text{SWAP}}$gate using a $\Lambda$ system, Phys. Rev. A **82**, 010301(R) (2010).

[4] S. Rosenblum, S. Parkins, and B. Dayan, Photon routing in cavity QED: Beyond the fundamental limit of photon blockade, Phys. Rev. A **84**, 033854 (2011).

[5] N. H. Lindner and T. Rudolph, Proposal for Pulsed On-Demand Sources of Photonic Cluster State Strings, Phys. Rev. Lett. **103**, 113602 (2009).

[6] I. Schwartz, D. Cogan, E. R. Schmidgall, Y. Don, L. Gantz, O. Kenneth, N. H. Lindner, and D. Gershoni, Deterministic generation of a cluster state of entangled photons, Science **354**, 434 (2016).

[7] N. Coste, D. A.Fioretto, N. Belabas *et al.*, High-rate entanglement between a semiconductor spin and indistinguishable photons, Nat. Photon. (2023).

[8] N. Tomm, A. Javadi, N. O. Antoniadis, D. Najer, M. C. Löbl, A. R. Korsch, R. Schott, S. R. Valentin, A. D. Wieck, A. Ludwig, and R. J. Warburton, A bright and fast source of coherent single photons, Nat. Nanotechnol. **16**, 399 (2021).

[9] R. J. Warburton, Single spins in self-assembled quantum dots, Nat. Mater. **12**, 483 (2013).

[10] I. Favero, G. Cassabois, R. Ferreira, D. Darson, C. Voisin, J. Tignon, C. Delalande, G. Bastard, P. Roussignol, and J. M. Gérard, Acoustic phonon sidebands in the emission line of single InAs/GaAs quantum dots, Phys. Rev. B **68**, 233301 (2003).

[11] A. V. Kuhlmann, J. H. Prechtel, J. Houel, A. Ludwig, D. Reuter, A. D. Wieck, and R. J. Warburton, Transform-limited single photons from a single quantum dot, Nat. Commun. **6**, 4 (2015).

[12] C. Santori, D. Fattal, J. Vučković, G. S. Solomon, and Y. Yamamoto, Indistinguishable photons from a single-photon device, Nature **419**, 594 (2002).

[13] Y. M. He, Y. He, Y. J. Wei, D. Wu, M. Atatüre, C. Schneider, S. Höfling, M. Kamp, C. Y. Lu, and J. W. Pan, On-demand semiconductor single-photon source with near-unity indistinguishability, Nat. Nanotechnol. **8**, 213 (2013).

[14] X. Ding, Y. He, Z.-C. Duan, N. Gregersen, M.-C. Chen, S. Unsleber, S. Maier, C. Schneider, M. Kamp, S. Höfling, C.-Y. Lu, and J.-W. Pan, On-Demand Single Photons with High Extraction Efficiency and Near-Unity Indistinguishability from a Resonantly Driven Quantum Dot in a Micropillar, Phys. Rev. Lett. **116**, 020401 (2016).

[15] N. Somaschi, V. Giesz, L. De Santis, J. C. Loredo, M. P. Almeida, G. Hornecker, S. L. Portalupi, T. Grange, C. Antón, J. Demory, C. Gómez, I. Sagnes, N. D. Lanzillotti-Kimura, A. Lemaítre, A. Auffeves, A. G. White, L. Lanco, and P. Senellart, Near-optimal single-photon sources in the solid state, Nat. Photon. **10**, 340 (2016).

[16] P. Senellart, G. Solomon, and A. White, High-performance semiconductor quantum-dot single-photon sources, Nat. Nanotechnol. **12**, 1026 (2017).

[17] P. Hilaire, C. Millet, J. C. Loredo, C. Antón, A. Harouri, A. Lemaître, I. Sagnes, N. Somaschi, O. Krebs, P. Senellart, and L. Lanco, Deterministic assembly of a charged-quantum-dot–micropillar cavity device, Phys. Rev. B **102**, 195402 (2020).

[18] M. Bayer, G. Ortner, O. Stern, A. Kuther, A. A. Gorbunov, A. Forchel, P. Hawrylak, S. Fafard, K. Hinzer, T. L. Reinecke, S. N. Walck, J. P. Reithmaier, F. Klopf, and F. Schafer, Fine structure of neutral and charged excitons

in self-assembled In(Ga)As/(Al)GaAs quantum dots, Phys. Rev. B **65**, 195315 (2002).

[19] R. Stockill, M. J. Stanley, L. Huthmacher, E. Clarke, M. Hugues, A. J. Miller, C. Matthiesen, C. Le Gall, and M. Atatüre, Phase-Tuned Entangled State Generation between Distant Spin Qubits, Phys. Rev. Lett. **119**, 010503 (2017).

[20] C. Emary, X. Xu, D. G. Steel, S. Saikin, and L. J. Sham, Fast Initialization of the Spin State of an Electron in a Quantum Dot in the Voigt Configuration, Phys. Rev. Lett. **98**, 047401 (2007).

[21] X. Xu, Y. Wu, B. Sun, Q. Huang, J. Cheng, D. G. Steel, A. S. Bracker, D. Gammon, C. Emary, and L. J. Sham, Fast Spin State Initialization in a Singly Charged InAs-GaAs Quantum Dot by Optical Cooling, Phys. Rev. Lett. **99**, 097401 (2007).

[22] X. Xu, B. Sun, P. R. Berman, D. G. Steel, A. S. Bracker, D. Gammon, and L. J. Sham, Coherent population trapping of an electron spin in a single negatively charged quantum dot, Nat. Phys. **4**, 692 (2008).

[23] X. Xu, W. Yao, B. Sun, D. G. Steel, A. S. Bracker, D. Gammon, and L. J. Sham, Optically controlled locking of the nuclear field via coherent dark-state spectroscopy, Nature **459**, 1105 (2009).

[24] P. Steindl, H. Snijders, G. Westra, E. Hissink, K. Iakovlev, S. Polla, J. A. Frey, J. Norman, A. C. Gossard, J. E. Bowers, D. Bouwmeester, and W. Löffler, Artificial Coherent States of Light by Multi-photon Interference in a Single-Photon Stream, Phys. Rev. Lett. **126**, 143601 (2021).

[25] M. Kroner, K. M. Weiss, B. Biedermann, S. Seidl, A. W. Holleitner, A. Badolato, P. M. Petroff, P. Öhberg, R. J. Warburton, and K. Karrai, Resonant two-color high-resolution spectroscopy of a negatively charged exciton in a self-assembled quantum dot, Phys. Rev. B **78**, 075429 (2008).

[26] D. Huber, B. U. Lehner, D. Csontosová, M. Reindl, S. Schuler, S. F. Covre Da Silva, P. Klenovský, and A. Rastelli, Single-particle-picture breakdown in laterally weakly confining GaAs quantum dots, Phys. Rev. B **100**, 235425 (2019).

[27] P. Androvitsaneas, A. B. Young, C. Schneider, S. Maier, M. Kamp, S. Höfling, S. Knauer, E. Harbord, C. Y. Hu, J. G. Rarity, and R. Oulton, Charged quantum dot micropillar system for deterministic light-matter interactions, Phys. Rev. B **93**, 241409(R) (2016).

[28] P. Androvitsaneas, A. B. Young, J. M. Lennon, C. Schneider, S. Maier, J. J. Hinchliff, G. S. Atkinson, E. Harbord, M. Kamp, S. Höfling, J. G. Rarity, and R. Oulton, Efficient quantum photonic phase shift in a low Q-factor regime, ACS. Photon. **6**, 429 (2019).

[29] C. Adambukulam, V. K. Sewani, H. G. Stemp, S. Asaad, M. T. Mądzik, A. Morello, and A. Laucht, An ultra-stable 1.5 T permanent magnet assembly for qubit experiments at cryogenic temperatures, Rev. Sci. Instrum. **92**, 085106 (2021).

[30] C. J. Fredricksen, E. W. Nelson, A. V. Muravjov, and R. E. Peale, High field p-Ge laser operation in permanent magnet assembly, Infrared Phys. Technol. **44**, 79 (2003).

[31] K. Tokuhara, Y. Ohtsu, F. Ono, O. Yamada, M. Sagawa, and Y. Matsuura, Magnetization and torque measurements on $Nd_2Fe_{14}B$ single crystals, Solid State Commun. **56**, 333 (1985).

[32] Y. Z. He, Experimental research on the residual magnetization of a rare-earth permanent magnet for a cryogenic undulator, Chin. Phys. B **22**, 074101 (2013).

[33] T. Hara, T. Tanaka, H. Kitamura, T. Bizen, X. Maréchal, T. Seike, T. Kohda, and Y. Matsuura, Cryogenic permanent magnet undulators, Phys. Rev. Accel. Beams **7**, 050702 (2004).

[34] M. Bayer, O. Stern, A. Kuther, and A. Forchel, Spectroscopic study of dark excitons in InGaAs self-assembled quantum dots by a magnetic-field-induced symmetry breaking, Phys. Rev. B **61**, 7273 (2000).

[35] T. Miyake and H. Akai, Quantum theory of rare-earth magnets, J. Phys. Soc. Jpn. **87**, 041009 (2018).

[36] C. Wang and M. G. Zhu, Overview of composition and technique process study on 2:17-type Sm-Co high-temperature permanent magnet, Rare Met. **40**, 790 (2021).

[37] J. Zhou, R. Skomski, C. Chen, G. Hadjipanayis, and D. Sellmyer, Sm-Co-Cu-Ti high-temperature permanent magnets, Appl. Phys. Lett. **77**, 1514 (2000).

[38] O. Gutfleisch, Controlling the properties of high energy density permanent magnetic materials by different processing routes, J. Phys. D. Appl. Phys. **33**, R157 (2000).

[39] O. Gutfleisch, M. A. Willard, E. Brück, C. H. Chen, S. G. Sankar, and J. P. Liu, Magnetic materials and devices for the 21st century: Stronger, lighter, and more energy efficient, Adv. Mater. **23**, 821 (2011).

[40] M. Duerrschnabel, M. Yi, K. Uestuener, M. Liesegang, M. Katter, H. J. Kleebe, B. Xu, O. Gutfleisch, and L. Molina-Luna, Atomic structure and domain wall pinning in samarium-cobalt-based permanent magnets, Nat. Commun. **8**, 54 (2017).

[41] K. Guo, H. Lu, G. J. Xu, D. Liu, H. B. Wang, X. M. Liu, and X. Y. Song, Recent progress in nanocrystalline Sm-Co based magnets, Mater. Today Chem. **25**, 100983 (2022).

[42] K. Durst, H. Kronmüller, F. T. Parker, and H. Oesterreicher, Temperature dependence of coercivity of cellular $Sm_2Co_{17}$-$SmCo_5$ permanent magnets, Phys. Status Solidi **95**, 213 (1986).

[43] L. Liu, Z. Liu, X. Zhang, C. Zhang, T. Li, D. Lee, and A. Yan, 2:17 type SmCo magnets with low temperature coefficients of remanence and coercivity, J. Magn. Magn. Mater. **473**, 376 (2019).

[44] See Supplemental Material at http://link.aps.org/supplemental/10.1103/PhysRevApplied.20.014026 for more details on the magnetic assembly simulations, sample design, derivation of the two-color-resonant-excitation model, and additional experiments.

[45] H. J. Snijders, D. N. Kok, M. F. Van De Stolpe, J. A. Frey, J. Norman, A. C. Gossard, J. E. Bowers, M. P. Van Exter, D. Bouwmeester, and W. Löffler, Extended polarized semiclassical model for quantum-dot cavity QED and its application to single-photon sources, Phys. Rev. A **101**, 053811 (2020).

[46] H. Snijders, J. A. Frey, J. Norman, V. P. Post, A. C. Gossard, J. E. Bowers, M. P. van Exter, W. Löffler, and D. Bouwmeester, Fiber-Coupled Cavity-QED Source of Identical Single Photons, Phys. Rev. Appl. **9**, 031002 (2018).

[47] D. Heiss, V. Jovanov, M. Bichler, G. Abstreiter, and J. J. Finley, Charge and spin readout scheme for single self-assembled quantum dots, Phys. Rev. B **77**, 235442 (2008).

[48] D. Heiss, V. Jovanov, F. Klotz, D. Rudolph, M. Bichler, G. Abstreiter, M. S. Brandt, and J. J. Finley, Optically monitoring electron spin relaxation in a single quantum dot using a spin memory device, Phys. Rev. B **82**, 245316 (2010).

[49] J. Frey, *Cavity Polarization Tuning for Enhanced Quantum Dot Interactions*. Ph.D. thesis, University of California, Santa Barbara (2019).

[50] P. Steindl, J. A. Frey, J. Norman, J. E. Bowers, D. Bouwmeester, and W. Löffler, Cross-Polarization-Extinction Enhancement and Spin-Orbit Coupling of Light for Quantum-Dot Cavity Quantum Electrodynamics Spectroscopy, Phys. Rev. Appl. **19**, 064082 (2023).

[51] A. J. Bennett, M. A. Pooley, Y. Cao, N. Sköld, I. Farrer, D. A. Ritchie, and A. J. Shields, Voltage tunability of single-spin states in a quantum dot, Nat. Commun. **4**, 1522 (2013).

[52] T. Nakaoka, T. Saito, J. Tatebayashi, and Y. Arakawa, Size, shape, and strain dependence of the g factor in self-assembled In(Ga)As quantum dots, Phys. Rev. B **70**, 235337 (2004).

[53] M. Kaniber, A. Laucht, A. Neumann, J. M. Villas-Bôas, M. Bichler, M. C. Amann, and J. J. Finley, Investigation of the nonresonant dot-cavity coupling in two-dimensional photonic crystal nanocavities, Phys. Rev. B - Condens. Matter Mater. Phys. **77**, 161303(R) (2008).

[54] J. Suffczyński, A. Dousse, K. Gauthron, A. Lemaître, I. Sagnes, L. Lanco, J. Bloch, P. Voisin, and P. Senellart, Origin of the Optical Emission within the Cavity Mode of Coupled Quantum Dot-Cavity Systems, Phys. Rev. Lett. **103**, 027401 (2009).

[55] M. Atatüre, J. Dreiser, A. Badolato, and A. Imamoglu, Quantum-dot spin-state preparation with near-unity fidelity, Science **312**, 551 (2006).

[56] R. Loudon, *The Quantum Theory of Light (Oxford Science Publications)* (Oxford University Press, USA, 1973), 3rd ed.

[57] N. Coste *et al.*, Quantum Sci. Technol. **8**, 025021 (2023).